Supporting Information

Experimental Section

1. Preparation of biodegradable and conducting fiber.

Biodegradable polyglycolic acid yarns (Bayen Healthcare Suzhou Co., Ltd.) were arranged on the glass slides and placed in the chamber of an ion sputtering instrument (Q150R, Quorum Technologies Ltd.) for gold sputtering. The sputtering current was set at 10 mA and the sputtering time was 15 min. The conducting fiber was then obtained by twisting multi-strand gold-coated biodegradable polyglycolic acid yarns.

2. Preparation of the fiber anode.

A 5.0 g/L dopamine solution was prepared with tris(hydroxymethyl) aminomethane hydrochloride buffer solution (pH of 8.5) as the solvent. A conducting fiber was then immersed in the above solution, followed by polymerization in air at 60 ℃ for 24 h. The resulting fiber was washed with deionized water and dried at 80 ℃ for 1 h. The fiber anode was then prepared by an electropolymerization process using a CHI660E electrochemical workstation at room temperature. Specifically, the conducting fiber coated with polydopamine was immerged in an aqueous electrolyte containing 0.1 M pyrrole and 0.1 M KNO_3 at a pH of ~3 as working electrode; platinum and saturated calomel electrode (SCE) were used as counter and reference electrodes, respectively. A constant potential of 0.7 V *vs.* SCE was used for a period of time to control the mass ratio of polydopamine and polypyrrole to 1:1. After electropolymerization, the fiber anode was washed with deionized water and dried at room temperature.

3. Preparation of the fiber cathode.

The fiber cathode was prepared by electrodeposition at room temperature using a CHI660E electrochemical workstation. To ensure the consistency of the degradation rate of the two fiber electrodes, the conducting fiber used to prepare the fiber cathode was also immersed in the same tris(hydroxymethyl) aminomethan hydrochloride buffer solution at 60 ℃ for 24 h before electrodeposition. The treated conducting fiber was immerged in an aqueous electrolyte containing 0.1 M $Mn(Ac)_2$ and 0.1 M Na_2SO_4 as

working electrode; platinum and Ag/AgCl electrodes were used as counter and reference electrodes, respectively. Then a pulse electrodeposition mode (1.5 V for 1 s and 0.7 V for 10 s) was used to electrodeposit MnO_2 on the conducting fiber. After electrodeposition, the fiber cathode was washed with deionized water and dried in air.

4. Fabrication and injection of the fiber battery.

Chitosan solution (4 wt%) was obtained by dissolving chitosan powder in acetic acid solution (2 wt%) under vigorous stirring at room temperature. Then the fiber cathode was coated with a layer of chitosan by dip-coating and dried at 80 ℃ for 30 minutes. Before battery assembly, the fiber anode was pre-loaded with Na^+ by electrochemical reduction to the potential of –0.4 V in 1× phosphate-buffered saline (1× PBS) with activated carbon and SCE as counter and reference electrodes, respectively. The fiber anode and cathode were twisted together to produce the fiber battery. As for injection, the fiber battery was firstly threaded through the needle (the diameter was slightly larger than the size of the fiber battery) of a syringe containing normal saline (0.9% NaCl solution). Then the needle was pricked into the target area, followed by injecting the syringe with an injection pressure of approximately 80 kPa while pulling it out of the body. The fiber battery could be successfully injected into the body under the driving effect of the normal saline.

5. Fabrication of the fiber sensor.

The fabrication of fiber sensor was summarized below. Spring-like fiber substrates (Zhiheng Co., Ltd.) were immersed in carbon nanotube conductive ink (weight concentration of 10%) under ultrasonic treatment for 15 min and then dried at 60 °C for 20 min. The resulting conductive fiber can directly serve as pressure sensor.

6. Degradation study of the fiber battery *in vitro*.

The fiber battery was immersed in 1× PBS at 37 °C for degradation evaluation. Its specific capacity was tested at current density of 1000 $mA \cdot g^{-1}$ every day until it failed to work. The fiber battery was dried in vacuum at room temperature and weighed every week to conduct a quantitative analysis of the weight loss upon increasing degradation time.

7. Electrochemical measurements.

The electrochemical properties of the fiber electrodes *in vitro* were tested in a three-electrode mode at room temperature, with activated carbon and SCE as the counter and reference electrodes respectively, and 1× PBS was employed as the electrolyte to simulate the humoral environment. Specifically, the galvanostatic charge/discharge, rate capability and cyclic performance of the fiber electrodes were tested on an Arbin electrochemical station (MSTATS-5 V/10 mA/16Ch), and the cyclic voltammograms were obtained by a CHI660E electrochemical workstation. The electrochemical properties of the fiber battery *in vitro* were measured using an Arbin electrochemical station (MSTAT-5 V/10 mA/16Ch) with 1× PBS as the electrolyte at room temperature. The electrochemical properties of the fiber battery *in vivo* were investigated by a CHI660E electrochemical workstation employing body fluid as electrolyte. The specific capacity (C) was calculated from the equation of $C = (I \times \Delta t)/m$, where I and Δt corresponded to the discharge current and discharge time, respectively. For the fiber anode and cathode, m was the weight of the active material on the corresponding fiber electrode. For the full fiber battery, m was the weight of the active material on the fiber anode.

8. Animals.

Six-week-old ICR white mice (female, about 20 g in weight) were purchased from Shanghai SLAC Laboratory Animal Co. All animal experiments were carried out in accordance with the protocols approved by the Animal Experimentation Committee of Fudan University, and all the animals were treated in accordance with guidelines for the care and use of experimental animals described by the National Institutes of Health and Fudan University.

9. Biocompatibility and biodegradation studies of the fiber battery.

The fiber batteries were injected into the abdominal subcutis of mice and regulated to different states of charge (voltage of 1.2 V, 0.6 V and 0 V) for experimental group, and nothing was implanted into the body of mice for control group. After four weeks, all the mice were euthanized. The subcutaneous tissues containing fiber batteries at different states of charge of the experimental group and the subcutaneous tissues at corresponding position of the control group were incised into small pieces (about 1×1

cm^2). They were then fixed with 4% (v/v) paraformaldehyde in 1× PBS solution at 4 °C and sliced into sections later with a thickness of about 4 μm using a microtome (Leica RM 2135, Leica Microsystems). Next, H&E staining, F4/80 and LY-6G immunofluorescence staining were conducted according to the standard procedures. For histopathology analysis, after the fiber batteries at different states of charge had been implanted for four weeks and fully biodegraded, the mice were euthanized, and the heart, liver, spleen, lung and kidney of the experimental and control groups were excised. They were then fixed and sliced into sections by the same way as above. Later, the H&E staining was carried out according to the standard procedure for further evaluation. The subcutaneous tissues at implantation sites were also excised, fixed and sliced into sections after the fiber batteries at different states of charge had completely biodegraded *in vivo*. Then H&E staining was performed to study whether there existed abnormalities of tissue morphology. As for biodegradation studies, the fiber batteries were injected into the abdominal subcutis of mice, and several mice were euthanized every two weeks to observe the biodegradation state of the fiber battery.

10. Characterization.

The morphologies were characterized by field-emission scanning electron microscopy (SEM, Zeiss FE-SEM Ultra 55). The electrical resistance was tested by a CHI660E electrochemical workstation (Shanghai Chenhua Instrument Co., Ltd.). The ionic conductivity was explored by using two stainless steel electrodes (area: 1×1 cm^2, distance: 0.5 cm) over a frequency range of 0.1 MHz to 0.1 Hz with 5 mV AC amplitude at room temperature. It was estimated as equation of $\sigma = D/(R \times A)$, where σ was the ionic conductivity ($S \cdot cm^{-1}$), D was the distance (cm) between the two electrodes, R was the ohmic resistance (Ω) and A was the area (cm^2) of the electrodes. The stiffness was measured with dynamic mechanical analyzer (Q800, TA instruments). Specifically, the samples were mounted with a single cantilever clamp and tested with a frequency sweep (0.01–10 Hz) under controlled displacement (50 μm) at 37 ℃. Electrochemical properties were studied by CHI660E electrochemical workstation and Arbin electrochemical station (MSTAT-5 V/10 mA/16Ch). The H&E staining and immunofluorescence staining sections were observed under a microscope (Olympus BX51). The photographs were taken by a digital camera (SONY A6000, Japan).

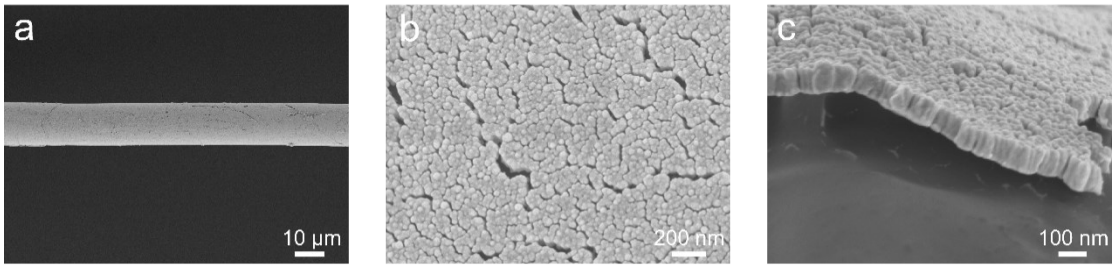

Figure S1. a, **b**, SEM images of the polyglycolic acid yarn coated with gold at low and high magnifications, respectively. **c**, Cross-sectional SEM image of the coated gold film.

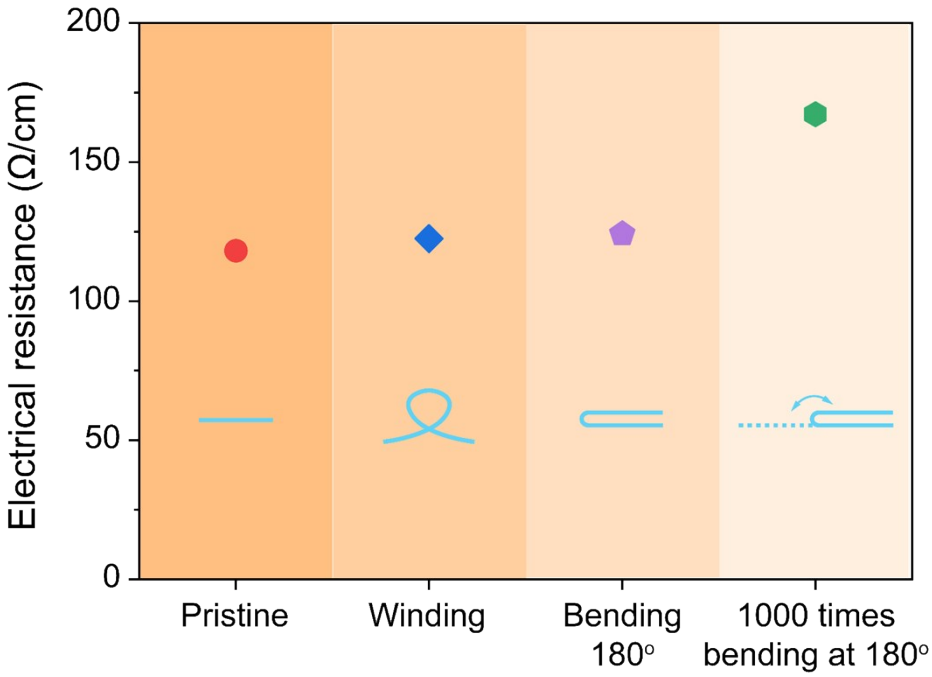

Figure S2. Electrical resistance of the polyglycolic acid yarn coated with gold at different deformation modes.

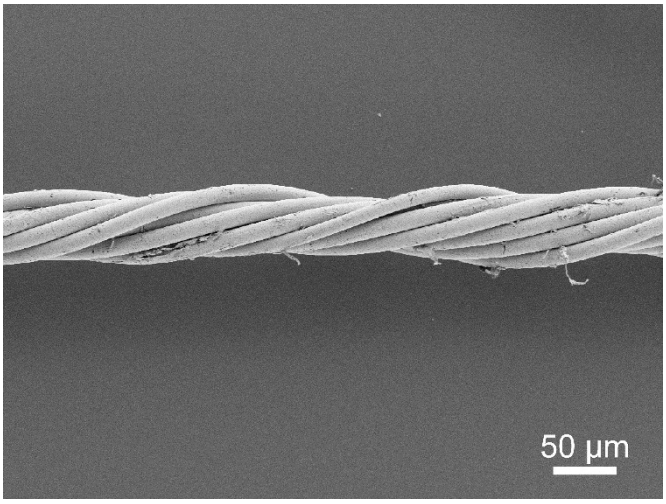

Figure S3. SEM image of the biodegradable and conducting fiber.

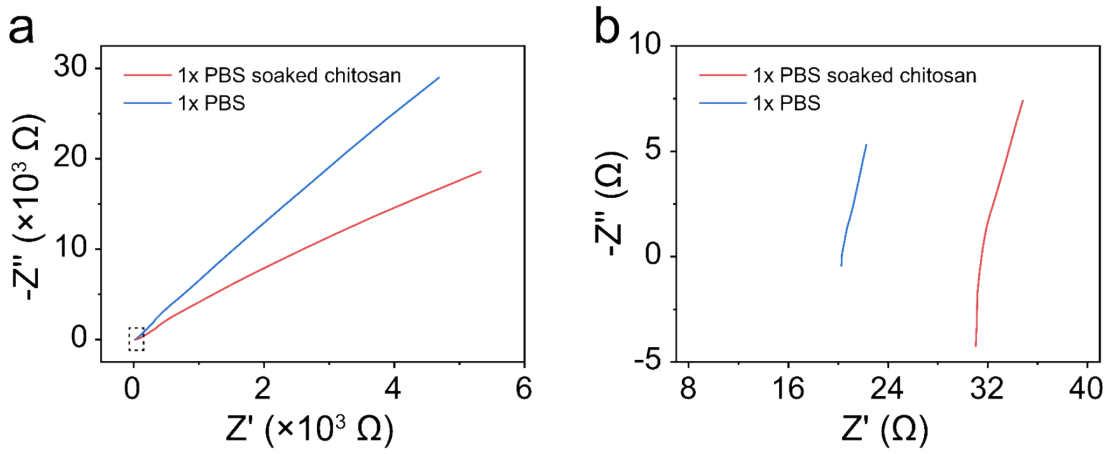

Figure S4. a, Nyquist plot of 1× PBS soaked chitosan and 1× PBS. **b**, Magnified part of the black dotted box in **a**.

Table S1. Ionic conductivity of 1× PBS soaked chitosan and 1× PBS at room temperature.

	1× PBS soaked chitosan	1× PBS
Ionic conductivity ($S \cdot cm^{-1}$)	1.59×10^{-2}	2.47×10^{-2}

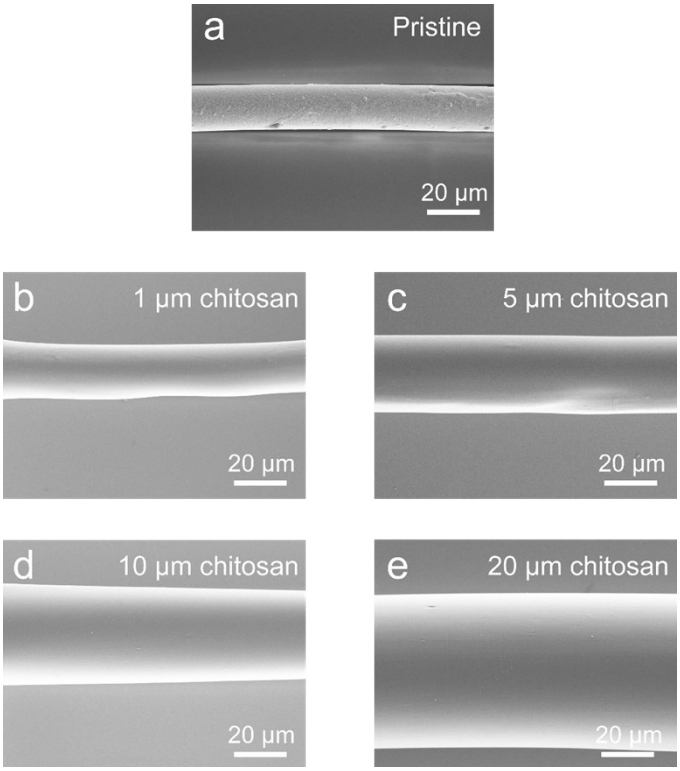

Figure S5. a, SEM image of the single cathode yarn. **b-e**, SEM images of the single cathode yarn dip-coated with chitosan with thickness of approximately 1, 5, 10 and 20 μm, respectively, demonstrating the controllable thickness of the chitosan separator.

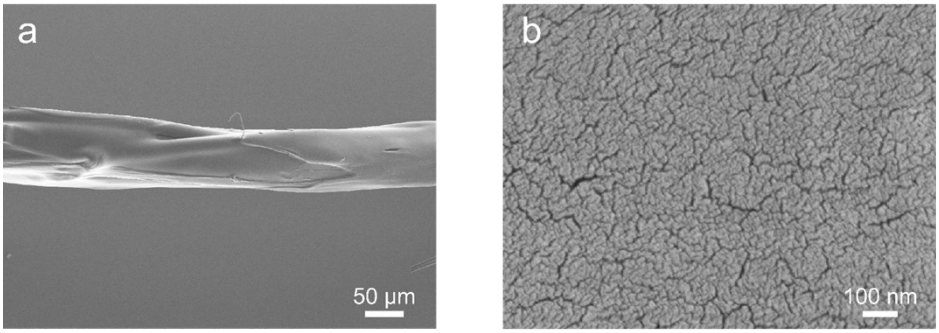

Figure S6. a, **b**, SEM images of the fiber cathode coated with chitosan with thickness of approximately 10 μm at low and high magnifications, respectively.

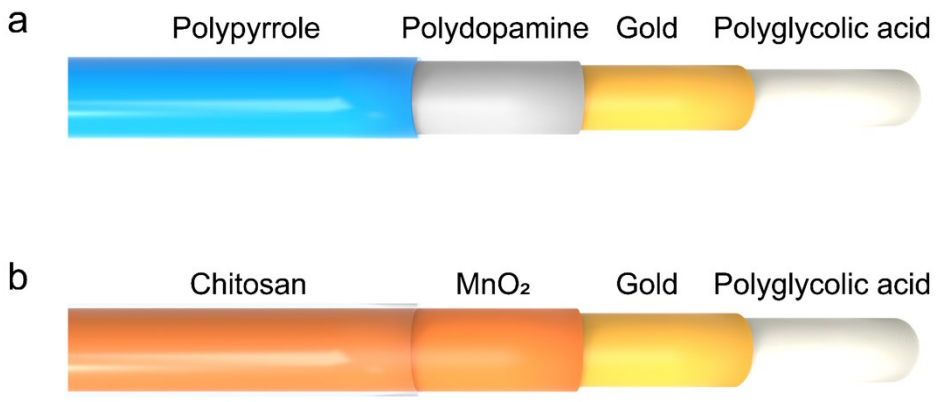

Figure S7. a, **b**, Structure and components of the fiber anode and cathode, respectively.

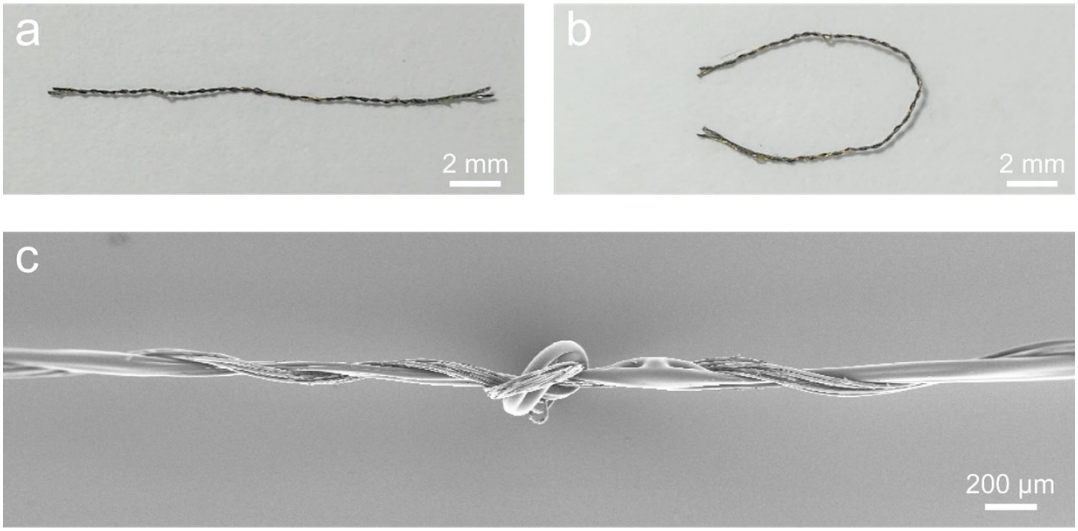

Figure S8. a, Photograph of an assembled fiber battery. **b**, Photograph of an assembled fiber battery bending at 180°. **c**, SEM image of a knotted fiber battery with high flexibility and robustness.

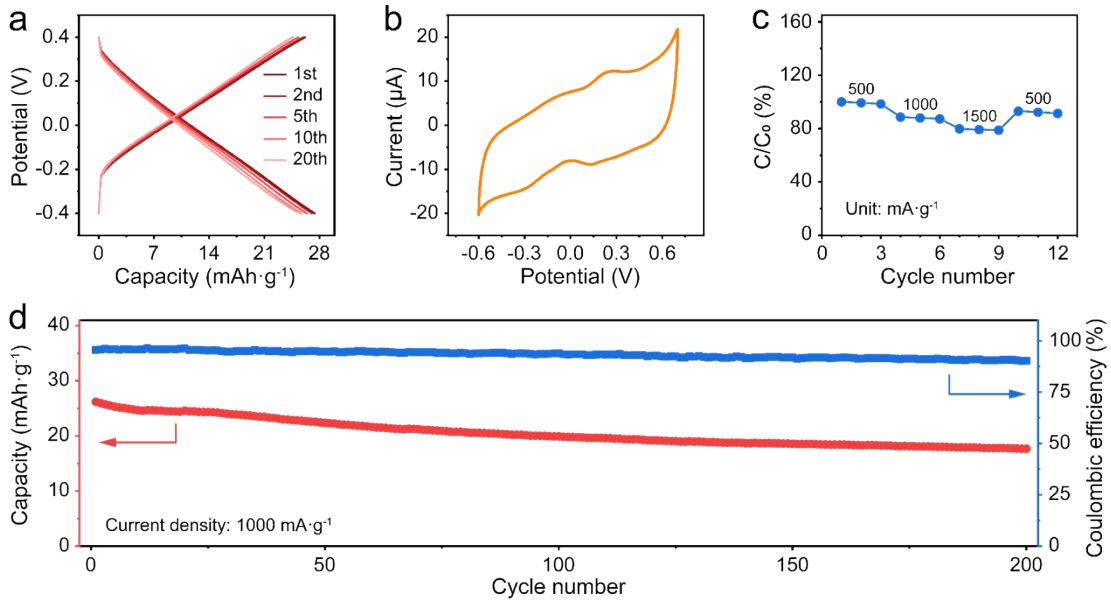

Figure S9. Electrochemical properties of the fiber anode *in vitro*. a, Galvanostatic charge and discharge profiles at current density of 1000 mA·g^{-1}. **b**, Cyclic voltammogram at scan rate of 0.1 V·s^{-1}. **c**, Rate capability at increasing current densities from 500 to 1500 mA·g^{-1}. **d**, Cycling performance at current density of 1000 mA·g^{-1}. All the tests were performed in a three-electrode mode in 1× PBS with activated carbon and SCE as counter and reference electrodes, respectively.

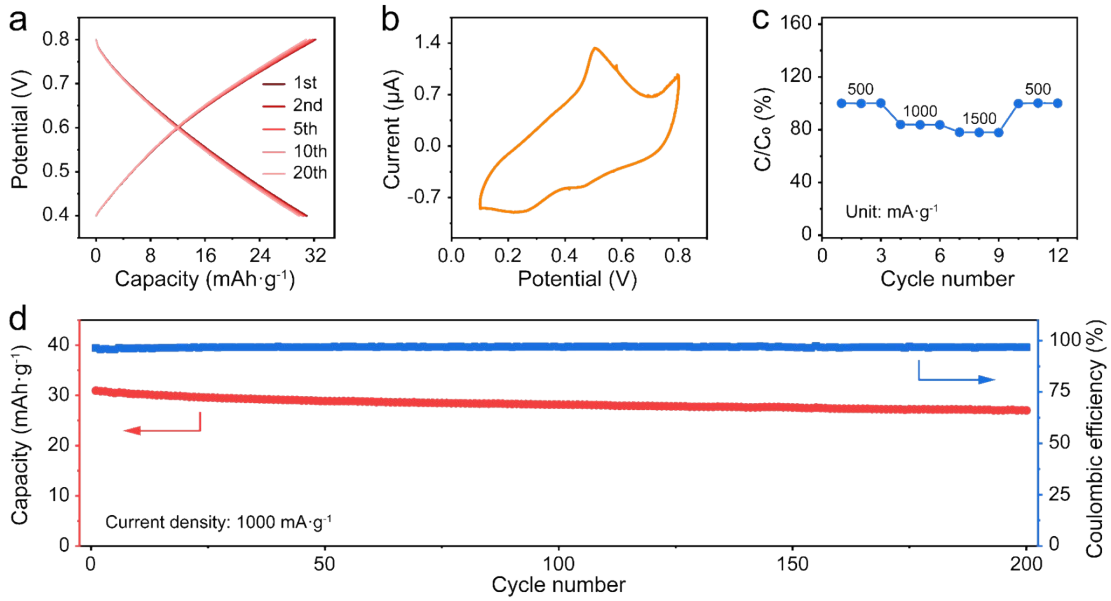

Figure S10. Electrochemical properties of the fiber cathode *in vitro*. **a**, Galvanostatic charge and discharge profiles at current density of 1000 mA·g^{-1}. **b**, Cyclic voltammogram at scan rate of 0.1 mV·s^{-1}. The redox peaks are attributed to the reversible faradic reaction of $MnO_2 + x\ H^+ + y\ Na^+ + (x + y)\ e^- \leftrightarrow MnOOH_xNa_y$. **c**, Rate capability at increasing current densities from 500 to 1500 mA·g^{-1}. **d**, Cycling performance at current density of 1000 mA·g^{-1}. All the tests were performed in a three-electrode mode in 1× PBS with activated carbon and SCE as counter and reference electrodes, respectively.

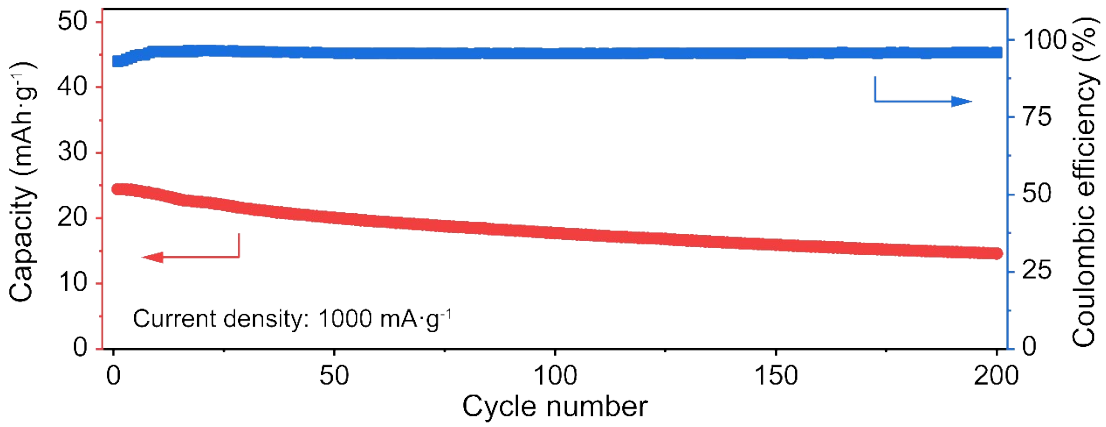

Figure S11. Cyclic stability of the fiber battery in 1× PBS.

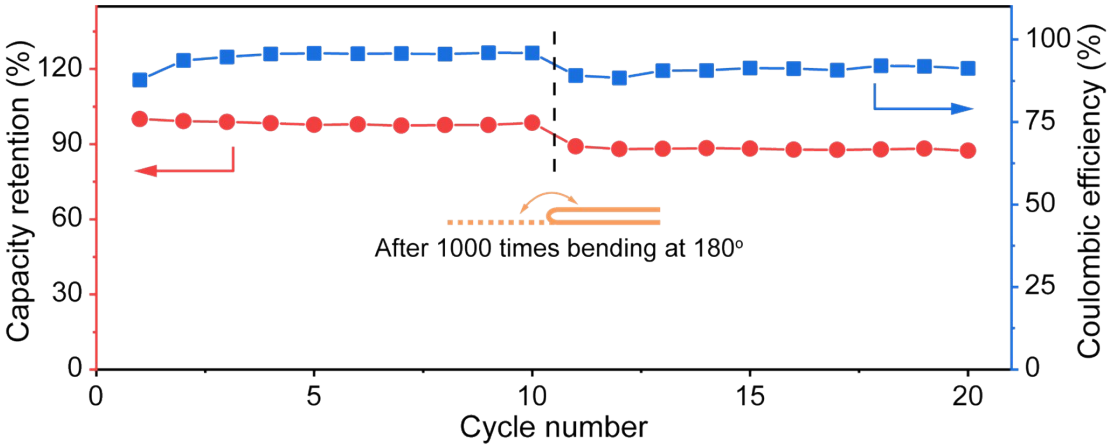

Figure S12. Capacity retention and coulombic efficiency of the fiber battery before and after 1000 bending cycles at bending angle of 180° at current density of 1000 $mA \cdot g^{-1}$.

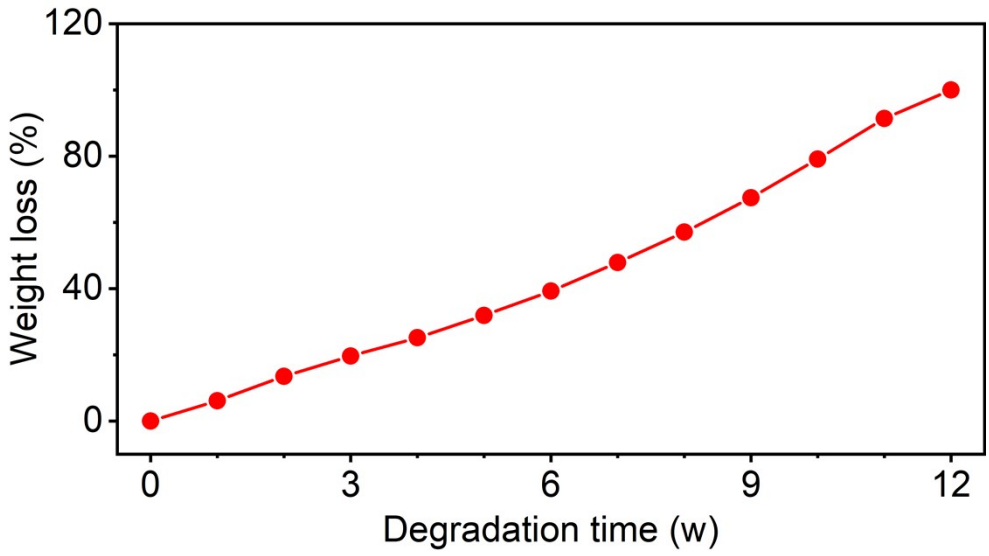

Figure S13. Evolution of weight loss upon increasing degradation time in 1× PBS at 37 °C.

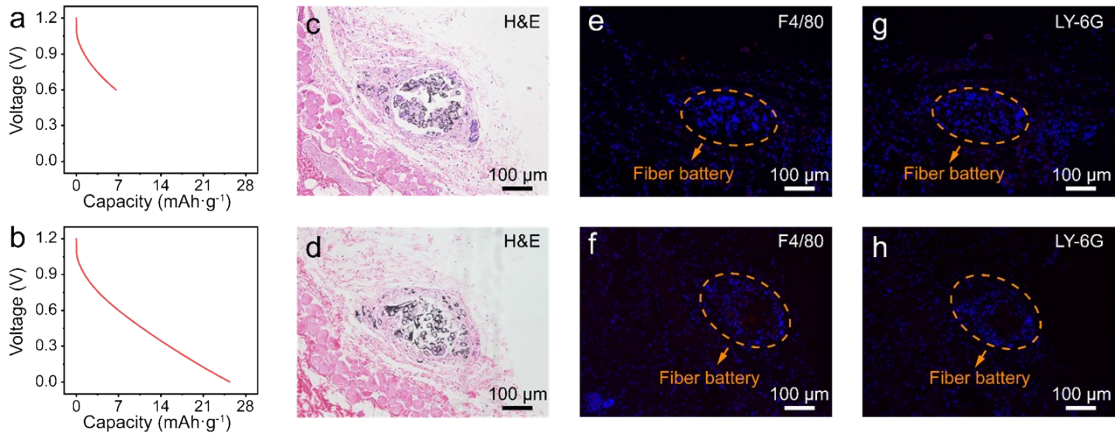

Figure S14. a, **b**, Galvanostatic discharge profiles at current density of 1000 mA·g^{-1} regulating voltage of the implanted fiber battery to 0.6 V and 0 V, respectively. **c**, **d**, Representative H&E sections of subcutaneous tissues with implantation of the fiber battery at voltage of 0.6 V and 0 V after 4 weeks, respectively. **e**, **f**, F4/80-labelled sections of subcutaneous tissues with implantation of the fiber battery at voltage of 0.6 V and 0 V after 4 weeks, respectively. The nucleus is shown in blue (DAPI) while F4/80 is shown in red. The orange dotted ellipse indicates the position of the fiber battery. **g**, **h**, LY-6G-labelled sections of subcutaneous tissues with implantation of the fiber battery at voltage of 0.6 V and 0 V after 4 weeks, respectively. The nucleus is shown in blue (DAPI) while LY-6G is shown in red. The orange dotted ellipse indicates the position of the fiber battery.

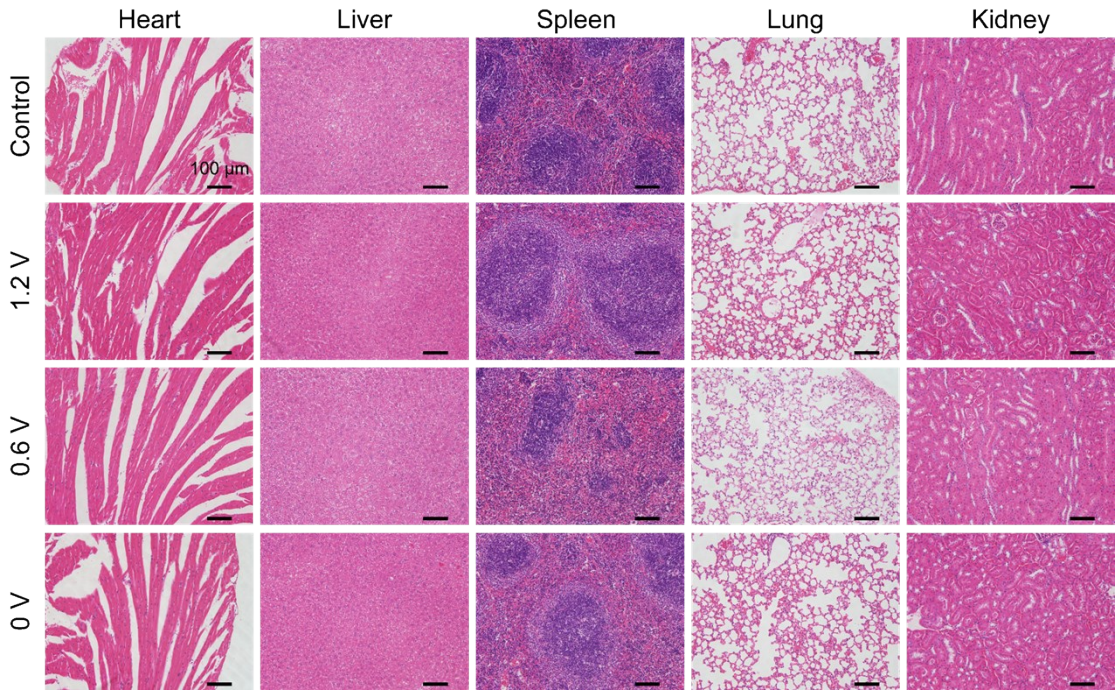

Figure S15. Representative H&E sections obtained from the major organs including heart, liver, spleen, lung and kidney of mice without and with implantation of the fiber batteries at different states of charge after 4 weeks.

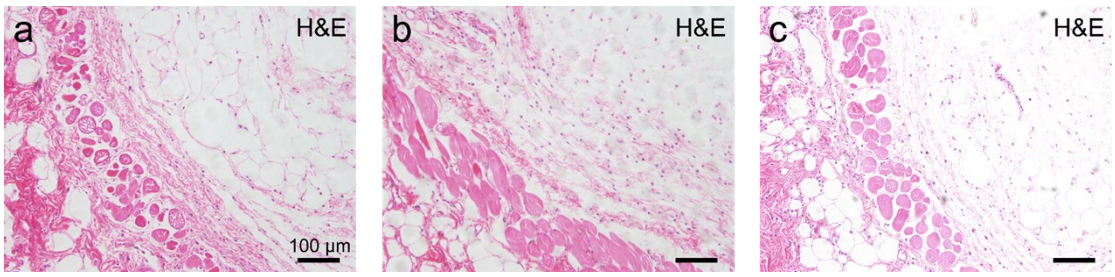

Figure S16. Representative H&E sections of subcutaneous tissues at implantation sites after the implanted fiber batteries at voltage of 1.2 V, 0.6 V and 0 V had completely biodegraded *in vivo*, respectively (**a-c**).

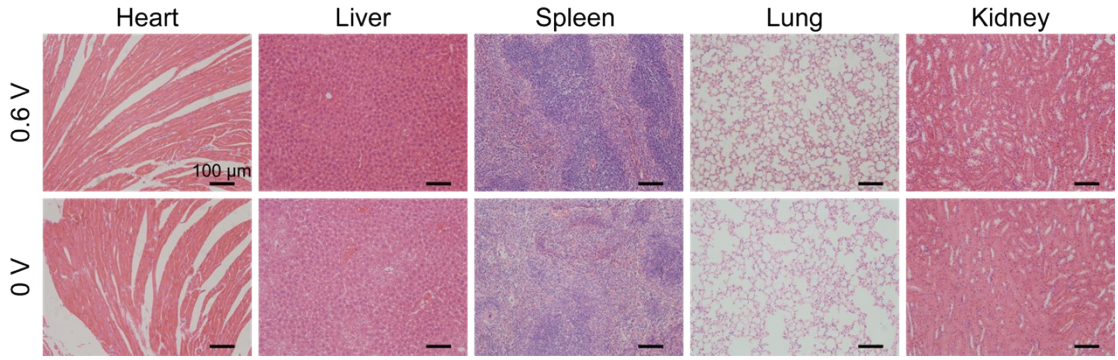

Figure S17. Representative H&E sections obtained from the major organs including heart, liver, spleen, lung and kidney of mice after the implanted fiber batteries at voltage of 0.6 V and 0 V had completely biodegraded *in vivo*.

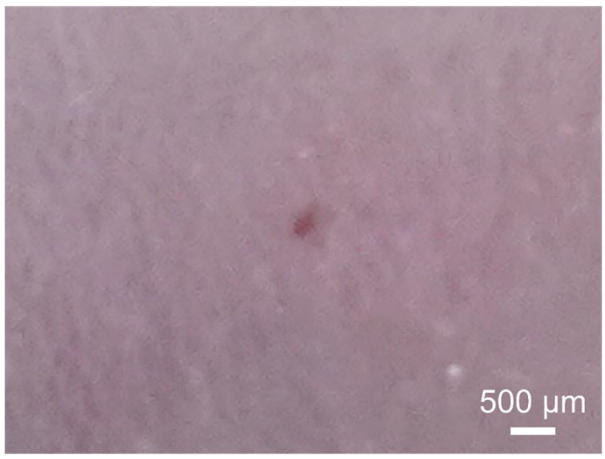

Figure S18. Photograph showing almost no wound after injection of the fiber battery.

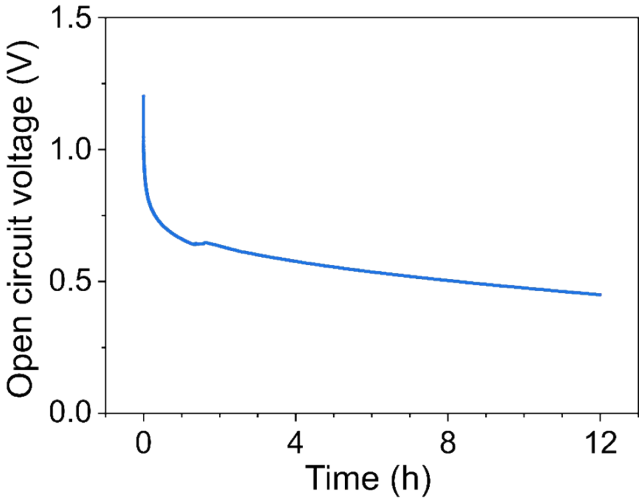

Figure S19. Open circuit voltage of the implanted fiber battery demonstrating no short circuits.

Table S2. Comparison of the fiber battery with the others.

Reference	Component	Configuration	Flexibility	Implantation method	Rechargeability
1	Mg-Mo	Bulky	Rigid	Surgery	No
2	Mg-Fe	Bulky	Rigid	Surgery	No
3	Mg-silk/polymer	Bulky	Rigid	Surgery	No
4	Mg-Au	Bulky	Rigid	Surgery	No
5	Zn-Cu	Bulky	Rigid	Surgery	No
6	Mg-MoO_3	Bulky	Rigid	Surgery	No
This work	**Polymer-MnO_2**	**Fiber**	**Flexible**	**Injection**	**Yes**

Supplementary References

1. L. Yin, X. Huang, H. Xu, Y. Zhang, J. Lam, J. Cheng, J. A. Rogers, *Adv. Mater.*, 2014, **26**, 3879–3884.
2. M. Tsang, A. Armutlulu, A. W. Martinez, S. A. B. Allen, M. G. Allen, *Microsystems Nanoeng.*, 2015, **1**, 15024.
3. X. Jia, C. Wang, C. Zhao, Y. Ge, G. G. Wallace, *Adv. Funct. Mater.*, 2016, **26**, 1454–1462.
4. X. Jia, C. Wang, V. Ranganathan, B. Napier, C. Yu, Y. Chao, M. Forsyth, F. G. Omenetto, D. R. Macfarlane, G. G. Wallace, *ACS Energy Lett.*, 2017, **2**, 831–836.
5. P. Nadeau, D. El-Damak, D. Glettig, Y. L. Kong, S. Mo, C. Cleveland, L. Booth, N. Roxhed, R. Langer, A. P. Chandrakasan, G. Traverso, *Nat. Biomed. Eng.*, 2017, **1**, 0022.
6. X. Huang, D. Wang, Z. Yuan, W. Xie, Y. Wu, R. Li, Y. Zhao, D. Luo, L. Cen, B. Chen, H. Wu, H. Xu, X. Sheng, M. Zhang, L. Zhao, L. Yin, *Small*, 2018, **14**, 1800994.